Journal of Advanced Ceramics
先进陶瓷
ISSN 2226-4108
CN 10-1154/TQ
清华大学出版社 Tsinghua University Press
SciOpen

J Adv Ceram 2026, **15**: 9221357

https://doi.org/10.26599/JAC.2026.9221357

Research Article

Multi-scale hardening and toughening of (Ti,Zr,V,Nb,Mo)C high-entropy carbides through coexisting phase separation and precipitation mechanisms

Zhixuan Zhang[1], Na Li[1], Zongyao Zhang[1], Jiatai Zhang[1], Qiang Zhang[1], Guorui Chang[1], Weili Wang[1], Weibin Zhang[1,2,*]

[1] *State Key Laboratory of Coatings for Advanced Equipment, Shandong University, Jinan 250061, China*

[2] *Shandong Key Laboratory of Advanced Structural Materials Genome Engineering, Shandong University, Jinan 250061, China*

* Corresponding author.

* E-mail addresses: zhangweibin@sdu.edu.cn

Received: March 18, 2026; Revised: July 1, 2026; Accepted: August 10, 2026

Abstract

The engineering application of transition metal carbides is often constrained by the inherent hardness-toughness trade-off. While phase modulation is an effective strategy, the intrinsic brittleness of ceramics still limits the achievable toughening. Taking (Ti, Zr, V, Nb, Mo)C high-entropy carbide as a model system, this work proposes a novel strategy to reconcile this trade-off by leveraging synergistic phase separation and precipitation. The as-sintered single-phase solid solution was subjected to optimized aging treatment, yielding a microstructure characterized by coexisting spinodal decomposition domains and precipitates. Specifically, a multi-scale synergistic strengthening mechanism is revealed. At the atomic scale, unique interface engineering combines semi-coherent spinodal interfaces with incoherent precipitate interfaces. This activates micro-scale defect engineering by inducing high-density dislocations, nano-twins, and stacking faults. This multi-scale system constructs a composite structure at the meso-scale where spinodal and precipitation domains coexist, effectively impeding dislocation motion and deflecting crack propagation. Driven by this mechanism, the material aged at 1300 °C for 20 h achieves an optimal synergy of properties, demonstrating concurrent increases in hardness (36%) and fracture toughness (45%) compared with the as-sintered state. This work opens a new avenue for designing advanced ceramic materials with superior damage tolerance.

Keywords: High-entropy carbide; Phase separation; Phase precipitation; Mechanical properties.

1. Introduction

High-entropy carbide ceramics are widely utilized in extreme service environments [1,2], including turbine blades in aerospace engines [3], ultra-high-temperature protective coatings [4], high-speed cutting tools [5], and structural components in nuclear reactors [6], owing to their exceptional hardness, wear resistance, and thermal stability [7-9]. However, this material system faces a significant challenge: the intrinsic hardness-toughness trade-off [10]. This trade-off leads to a significant reduction in their service life under harsh conditions such as abrasion, impact, and high temperatures, thereby limiting their further performance enhancement and broader application [11]. Traditional approaches often struggle to optimize these mutually exclusive properties simultaneously, mandating the development of innovative strategies to effectively address this issue.

Among the various microstructural engineering strategies, leveraging the spinodal decomposition mechanism during metastable phase transformation is a proven and effective pathway [12]. Spinodal decomposition is a spontaneous, continuous phase separation process that requires no nucleation barrier, resulting in a nano-scale, three-dimensional (3D) interconnected network structure of two interpenetrating phases within the solid solution matrix [13-15]. The semi-coherent interfaces, with their associated coherency strain fields and misfit dislocations, effectively impede dislocation motion, while the dense interfacial network can deflect crack propagation [16]. The hardening and toughening effects of spinodal decomposition have been preliminarily validated in several material systems, such as (Ti, Zr)C [10], (Ti, Hf)C [17], (Ti, Zr, Hf)C [18], and (Ti, Zr)(C, N) [19]. Nevertheless, when relying solely on the spinodal decomposition strategy, the achievable toughening is often constrained by the intrinsic brittleness of ceramic materials, hindering significant breakthroughs in toughness [20,21].

Moreover, as the number of system components increases, the free energy landscape becomes exceptionally complex, rendering the prediction and identification of specific compositional windows for spinodal decomposition extremely difficult by traditional methods [18].

To overcome the toughening limitations of the singular spinodal decomposition mechanism, this study proposes a novel strategy: the synergistic combination of spinodal decomposition and precipitation strengthening. Precipitation strengthening is another classic and highly effective strengthening mechanism, which operates by impeding dislocation motion via dispersed second-phase particles, typically featuring incoherent interfaces with the matrix [22-25]. The recently emerged concept of high-entropy ceramics, by dissolving multiple elements in high concentrations within a single crystal lattice, has vastly expanded the compositional design space for materials [26-28]. This provides an unprecedented platform for the synergistic modulation of these two mechanisms [29]. Phase separation phenomena previously observed in similar systems, such as (Ti, Zr)C [10] and (Ti, Zr, Hf)C [18], have demonstrated the feasibility of tailoring carbide microstructures via heat treatment. In this study, the high-entropy design involving multiple principal elements significantly broadens the thermodynamic tuning window, enabling the simultaneous activation of continuous spinodal decomposition and discontinuous precipitation transformations within a single system. The coupling of these multiple phase transformation mechanisms provides a new physical pathway for constructing multi-scale interface structures, thereby breaking the hardness-toughness trade-off. Therefore, determining whether these two metastable phase transformations can be simultaneously activated in a carefully designed high-entropy ceramics system—and subsequently elucidating their synergistic principles across different scales, revealing their intrinsic relationship, and constructing a hierarchical

strengthening microstructure—constitutes a frontier topic of significant scientific importance. It is a key step toward the rational design of materials with superior performance.

To address these issues, the (Ti, Zr, V, Nb, Mo)C quinary high-entropy carbide was selected as a model system to investigate the coupled evolution of phase separation and precipitation during aging. The main objective of this study is to clarify whether these two phase-transformation pathways can be activated and regulated within a single high-entropy carbide matrix, and how their coexistence affects the hardness-toughness balance. To this end, aging treatments were designed based on thermodynamic phase-stability analysis and preliminary experiments, followed by systematic characterization of phase evolution, interfacial structure, defect formation, and mechanical properties. Particular attention was paid to the relationship between phase-transformation-induced microstructures and the simultaneous changes in hardness and fracture toughness. This study aims to provide a clearer understanding of how coupled phase separation and precipitation can be used to regulate the mechanical response of high-entropy carbide ceramics.

2. Experimental and computational procedures

2.1 Materials preparation

High-purity commercial powders were used as raw materials, including: TiC (99%, 300–500 nm, Macklin Co. Ltd.), ZrC (99.9%, 400 nm–1 μm, Macklin Co. Ltd.), VC (99%, 500 nm–1 μm, Macklin Co. Ltd.), NbC (99% purity, 400 nm–1 μm, Macklin Co. Ltd.), Mo_2C (99.5% purity, 500 nm–1 μm, Macklin Co. Ltd.), and graphite C powder (99.5%, Macklin Co. Ltd.). The raw powders were weighed precisely according to the equiatomic ratio for (Ti, Zr, V, Nb, Mo)C. The powders were loaded into a

steel milling jar with WC milling balls (at a ball-to-powder ratio of 10:1), using anhydrous ethanol as the solvent. High-energy ball milling was performed for 36 hours at 400 rpm in a planetary ball mill to achieve sufficient mechanical mixing and refinement. The resulting slurry was dried in a vacuum oven (60 °C, 12 h) to completely remove the ethanol. The homogeneously mixed powders were then loaded into a graphite die with an inner diameter of 20 mm. Densification was carried out using a Spark Plasma Sintering (SPS) furnace (SPS-332HF, Fuji Electronics). The samples were heated to 2200 °C at a rate of 100 °C/min under a flowing argon atmosphere. A uniaxial pressure of 40 MPa was applied during the heating ramp and held for 10 min at the peak temperature of 2200 °C. This procedure aimed to fabricate high-density, chemically homogeneous single-phase solid solution ceramic bulks. After sintering, the sample was furnace-cooled to room temperature.

The aging parameters were designed based on thermodynamic phase-fraction calculations and preliminary experiments. The phase-fraction calculation was performed using Thermo-Calc software [30] with the CSUTDCC1 [31] thermodynamic database. As shown in **Figure S1** and discussed in **Section S1**, the high-temperature FCC carbide solid solution becomes thermodynamically unstable under the aging temperature range, providing the basis for selecting the aging window. Therefore, aging temperatures of 1100, 1200, 1300, 1400, and 1500 °C and aging durations of 10, 20, and 50 h were selected to capture the microstructural evolution from the early stage of phase transformation to developed phase separation and subsequent coarsening. Accordingly, the as-sintered dense bulk samples were cut into small pieces for aging treatment. The aging heat treatment was conducted in a tube furnace (Kejing GSL-1750X) under a flowing argon atmosphere. The samples were heated at a rate of 5 °C/min to 1100, 1200, 1300, 1400, or 1500 °C and held for 10, 20, or 50 h, respectively. After

aging, all samples were furnace-cooled to room temperature. The sample surfaces were then ground and polished for subsequent microstructural characterization and mechanical property testing.

2.2 Materials characterization

Phase identification was carried out using X-ray diffraction (XRD; Rigaku SmartLab) with a scanning rate of 10 °/min. Microstructural observations and compositional analyses were performed with a scanning electron microscope (SEM; JSM-7800F) equipped with energy-dispersive X-ray spectroscopy (EDS; Oxford XMax 80). The precipitate size was measured from SEM images using ImageJ software. For each aging condition, precipitates in the analyzed images were measured, and the average value was used as the representative particle size. Additional high-resolution microstructural observations were obtained via transmission electron microscopy (TEM; Thermofisher Talos F200X G2). The C and O elemental contents were determined using a carbon/sulfur analyzer (LECO CS844) and an oxygen/nitrogen/hydrogen analyzer (LECO ONH836). Vickers hardness (H_V) and fracture toughness (K_{IC}) measurements were conducted at room temperature using a Vickers hardness tester (HV-30A, Laizhou Huayu Zhongxin Testing Instrument Co., Ltd.) with a load of 9.8 N and a dwell time of 15 s. The fracture toughness K_{IC} was calculated based on **Equation (1)** [32]:

$$K_{IC} = 0.016 * \left(\frac{E}{H_V}\right)^{\frac{1}{2}} * \frac{P}{c^{\frac{3}{2}}} \quad (1)$$

where E is Young's modulus, H_V is the hardness value, P is the applied load, and c represents the half-length of cracks formed at the indentation corners. The modulus E was obtained from first-principles calculations. The elastic modulus employed for the K_{IC} calculation is 491 GPa. Given the high similarity in the moduli of the constituent carbides, and considering that E is an intrinsic property governed by interatomic bonding, it remains insensitive to microstructural defects such as dislocations

and twins. Consequently, adopting the calculated intrinsic modulus effectively mitigates experimental measurement errors and accurately reflects the elastic response of the multiphase composite microstructure [33]. This methodological approach has been widely validated and applied in studies involving phase decomposition and multiphase systems [13,34,35].

2.3 Ab initio calculations

First-principles calculations were performed to evaluate the twin-boundary energy and stacking-fault energy of ZrC with different C-vacancy concentrations. The calculations were carried out within the DFT framework using the Vienna ab initio simulation package (VASP) [36]. The interaction between valence electrons and ionic cores was described by the projector augmented wave (PAW) method [37], and the exchange–correlation energy was treated using the generalized gradient approximation (GGA) with the Perdew–Burke–Ernzerhof (PBE) functional [38]. The plane-wave kinetic energy cut-off was set to 520 eV, and the electronic self-consistent convergence criterion was set to 1×10^{-7} eV. For Brillouin zone integration, Gamma-centered k-point meshes were adopted, and a $5 \times 5 \times 1$ k-point mesh was used for the stacking-fault and twin-boundary supercells. B1-type rock-salt ZrC was used as the representative model. A 96-atom vacancy-free ZrC reference model was constructed, and ZrC_{1-x} supercell models with C-vacancy concentrations of 2%, 4%, and 8% were further established to simulate the possible C non-stoichiometry in the ZrC-rich precipitates. For each C-vacancy concentration, a planar-defect-free reference model, a (111) twin-boundary model, a (111) stacking-fault model, and a (100) stacking-fault model were constructed. The twin-boundary energy and stacking-fault energy were calculated from the total-energy differences between the corresponding defect-containing models and the reference models. To ensure the comparability of energies among

different models, the defect-containing models and their corresponding reference models were constructed with the same C-vacancy concentration, supercell size, and computational parameters.

3. Results and Discussion

3.1 Phase and Microstructural Evolution

To characterize the phase composition of the synthesized samples, XRD analysis was performed. **Figure 1** presents the XRD pattern of the as-sintered (Ti, Zr, V, Nb, Mo)C high-entropy ceramic. Only one set of sharp diffraction peaks is present in the pattern. All peaks correspond well with the standard card for the face-centered cubic (FCC) rock-salt structure (e.g., PDF#01-071-6256-TiC), and no diffraction peaks from any other impurity phases are observed. This indicates that the as-sintered sample formed a single-phase FCC solid solution structure [34,39]. Notably, the diffraction peaks of the (Ti, Zr, V, Nb, Mo)C solid solution are located between those of the individual carbides. The SEM micrographs in **Figure S2** reveal a dense and homogeneous microstructure for the as-sintered sample, with EDS mapping confirming a homogeneous elemental distribution. Furthermore, quantitative analysis using carbon/sulfur and oxygen/nitrogen/hydrogen analyzers (**Table S1**) confirms an extremely low oxygen content, indicating negligible oxidation in the as-sintered sample. This is a typical characteristic indicating the successful formation of a solid solution from all five metal elements [40], thereby confirming the successful synthesis of the material.

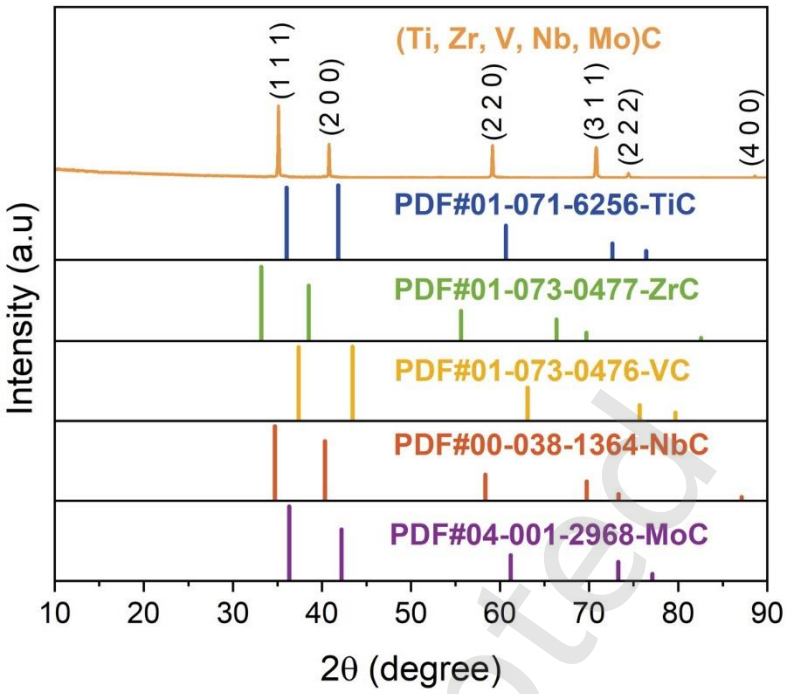

Figure 1. XRD pattern of the as-sintered (Ti, Zr, V, Nb, Mo)C high-entropy ceramic.

To elucidate the influence of aging parameters on the synergistic phase transformation, this study systematically investigated the microstructural evolution of (Ti, Zr, V, Nb, Mo)C high-entropy ceramics under various aging temperatures and durations. **Figure 2** shows the SEM-BSE (Back-Scattered Electron) micrographs of the samples aged in the temperature range of 1100 to 1500 °C for 10, 20, and 50 h. It should be noted that the phase-fraction diagram in **Figure S1** is used to describe the equilibrium phase-separation tendency of the high-temperature FCC solid solution. It predicts the separation of the matrix into (Ti, V, Mo)C-rich and (Zr, Nb)C-rich carbide phases during aging. The ZrC-rich precipitates observed in the SEM and TEM images are experimentally identified precipitates formed during finite-time aging. Their formation originates from local Zr enrichment in the supersaturated FCC solid solution, which is promoted by the Zr-related mixing instability during phase separation. When the local Zr concentration exceeds the solubility accommodated by the surrounding carbide matrix, ZrC-rich precipitates form from the supersaturated solid solution.

All aged samples exhibit coupled evolution of phase separation and precipitation, although the transformation extent varies with aging temperature and time [7,15,41]. At 1100 °C, the phase transformation proceeds slowly, and the microstructure remains mainly dominated by the supersaturated solid solution matrix. With increasing aging time, discrete ZrC-rich precipitates gradually appear and coarsen, whereas a continuous spinodal decomposition structure is not clearly developed. When the aging temperature is increased to 1200 °C, the phase transformation becomes more active. After aging for 10 h, weak local contrast fluctuations can be observed, suggesting the onset of early-stage phase decomposition. This is further supported by the TEM characterization shown in **Figure S3** and discussed in detail in **Section S2**, where fine spot-like contrast features are observed. At this stage, the phase decomposition remains in its early stage and has not yet evolved into a well-developed continuous spinodal structure. With further aging, the contrast modulation becomes more pronounced, accompanied by the progressive growth of ZrC-rich precipitates.

At 1300 °C, the microstructural evolution is more pronounced. A distinct coexisting structure is already formed after 10 h. As the aging time extends to 20 and 50 h, the phase-separated structure, originating from the grain boundaries, gradually expands into the grain interior. Meanwhile, the size and quantity of precipitates increase, forming an interwoven composite microstructure of the two features. Concurrently, the dispersed deep-black precipitates within the grains have coarsened to approximately 1 μm. When the temperature is further increased to 1400 °C, the transformation kinetics accelerate sharply. A phase-separated network penetrating the entire grain forms after only 10 h. With prolonged time, both this network structure and the precipitates begin to show clear signs of coarsening, indicating that the phase separation has entered an advanced stage.

At 1500 °C, the high-temperature-induced phase coarsening phenomenon (Ostwald ripening) becomes dominant [42-44]. Even after 10 h, the lamellar spacing of the spinodal structure and the average size of the precipitates are significantly larger than those in the 1300 and 1400 °C samples. When extended to 50 h, the microstructure presents an over-coarsened state, with the precipitates reaching 3.4 μm. In summary, the SEM results clearly reveal the coexistence and evolutionary behavior of the two phase transformation mechanisms—phase separation and precipitation—in the (Ti, Zr, V, Nb, Mo)C system. It is also demonstrated that by regulating the aging temperature and time, the scale of the phase separation can be precisely controlled, providing an experimental foundation for obtaining a hierarchical strengthening microstructure [45].

Representative samples were selected for EDS characterization, and the results, as illustrated in **Figure S4**, reveal that all observed precipitates exhibit distinct Zr enrichment. Coupled with quantitative elemental analysis showing negligible oxygen content, these precipitates are identified as ZrC-rich precipitates. Furthermore, systematic XRD analysis was conducted on samples across the full range of aging temperatures and times (**Figure S5**). The results indicate that, aside from the two phases resulting from the spinodal decomposition of the matrix and the ZrC-rich precipitates, no impurity peaks were detected in the diffraction patterns. This demonstrates that under the investigated heat treatment conditions, the phase transformation process involves only the anticipated phase separation and precipitation behaviors, without detectable oxide-related impurity phases within the resolution of XRD, thereby ensuring the chemical stability and phase purity of the high-entropy carbide system during high-temperature evolution.

To further quantitatively analyze the coarsening behavior of the precipitates, statistical

measurements of precipitate sizes under different temperatures and aging times were conducted using ImageJ software based on SEM images, and the results are shown in **Figure S6(a)**. It can be seen that within the range of 1100–1500 °C, the average precipitate size gradually increases with aging time. According to the classical Lifshitz–Slyozov–Wagner theory [46], in diffusion-controlled Ostwald ripening, the average precipitate radius satisfies:

$$r^3 - r_0^3 = Kt \tag{2}$$

Based on this relation, the curve of the cube of the precipitate size versus aging time was plotted, as shown in **Figure S6(b)**. During the aging process, r^3 exhibits an approximately linear relationship with time, indicating that the experimental results are consistent with the kinetic characteristics of Ostwald ripening.

Microstructural evolution reveals the activation sequence and distinct contributions of the two mechanisms across different temperatures. In the low-temperature regime, the precipitation mechanism is activated first, driven by the strong precipitation tendency. As the temperature increases, spinodal decomposition is rapidly initiated, establishing spatial synergy with the precipitate phases [47]. The transition in mechanical properties from a monotonic increase to a peak-and-decline trend reflects a dynamic balance between strengthening mechanisms and microstructural coarsening: the low-temperature regime is characterized by incomplete transformation due to sluggish kinetics, whereas the high-temperature regime exhibits performance degradation caused by Ostwald ripening and dislocation annihilation following rapid phase transformation. Ultimately, the long-range dislocation networks constructed via spinodal decomposition and the short-range strengthening sites provided by the precipitates jointly govern the macroscopic performance limits of the material [48].

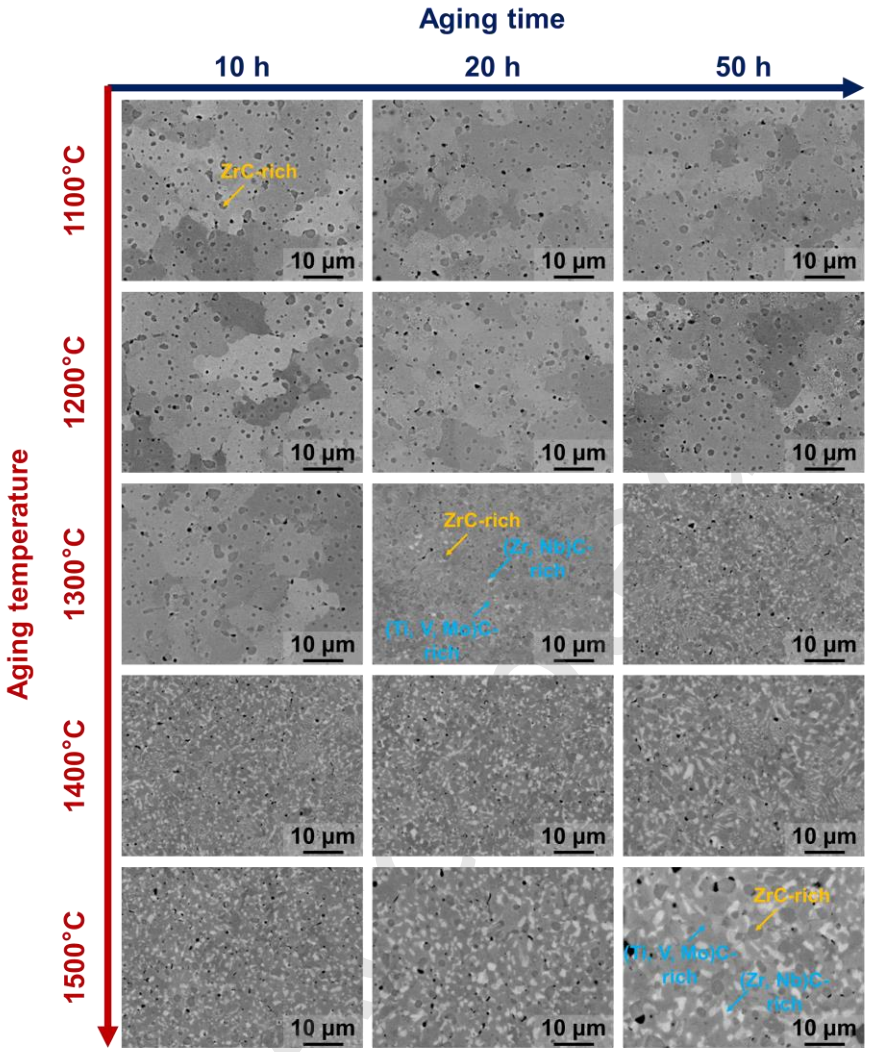

Figure 2. SEM-BSE micrograph evolution of (Ti, Zr, V, Nb, Mo)C high-entropy ceramics after aging heat treatment at different temperatures (1100–1500 °C) and for various durations (10, 20, 50 h).

The phase evolution of this quinary system is governed by the competition between the enthalpy of mixing and the configurational entropy. During sintering at 2200 °C, the high configurational entropy stabilizes the single-phase solid solution. However, within the aging temperature range of 1100–1500 °C, the entropic contribution diminishes, and the positive enthalpy of mixing—arising from atomic size mismatches and chemical incompatibilities between sublattices—begins to dominate. This thermodynamic instability drives the system into a miscibility gap, triggering spontaneous spinodal decomposition, while the high chemical potential gradients of specific components further induce the

precipitation and growth of secondary precipitates [48].

To elucidate the relationship between grain structure and defect evolution during the aging process, EBSD analysis was conducted on the samples aged for 20 h (**Figure 3**). The Inverse Pole Figure (IPF) map (**Figure 3(a, d, g, j, m)**) reveals that, unlike conventional ceramics which typically undergo grain coarsening during high-temperature heat treatment, the grain size of the present system did not significantly increase after aging between 1100 and 1500 °C. Instead, it exhibited an abnormal grain refinement trend. This is primarily attributed to the synergistic phase decomposition process involving the spinodal decomposition phases and ZrC-rich precipitates, which introduced significant lattice mismatch and internal stress fields [49-51]. This high level of internal stress not only suppressed the migration of existing grain boundaries via the Zener pinning effect but also induced the formation of new sub-grain boundaries, thereby leading to this abnormal grain refinement phenomenon [52,53].

Figure 3(b, e, h, k, n) presents the Kernel Average Misorientation (KAM) map and its distribution, which reflects the degree of lattice distortion. The density of Geometrically Necessary Dislocations (GNDs) is positively correlated with the average KAM value (KAM_{ave}). It is clear from the KAM distribution that the KAM_{ave} value exhibits a significant non-monotonic trend with increasing aging temperature, where it first increases and then decreases. It reaches a peak value at 1300 °C—significantly higher than that of the 1100 and 1200 °C samples—before gradually decreasing at 1400 and 1500 °C.

This trend strongly suggests that within the optimal aging window (1200–1300 °C), the simultaneous occurrence of spinodal decomposition and precipitation generates immense internal stress. This stress arises from the significant lattice and thermal mismatch between the new phases and

the matrix, and is subsequently relieved via plastic relaxation through the generation of high-density dislocations [54,55]. Conversely, at excessively high temperatures (≥1400 °C), the decrease in GND density is attributed to two factors: on one hand, microstructural coarsening reduces the phase transformation driving force and the degree of lattice mismatch [56]; on the other hand, the high temperature accelerates the recovery and annihilation of dislocations. This evolutionary trend of high-density dislocations significantly influences the material's hardness and toughness [57].

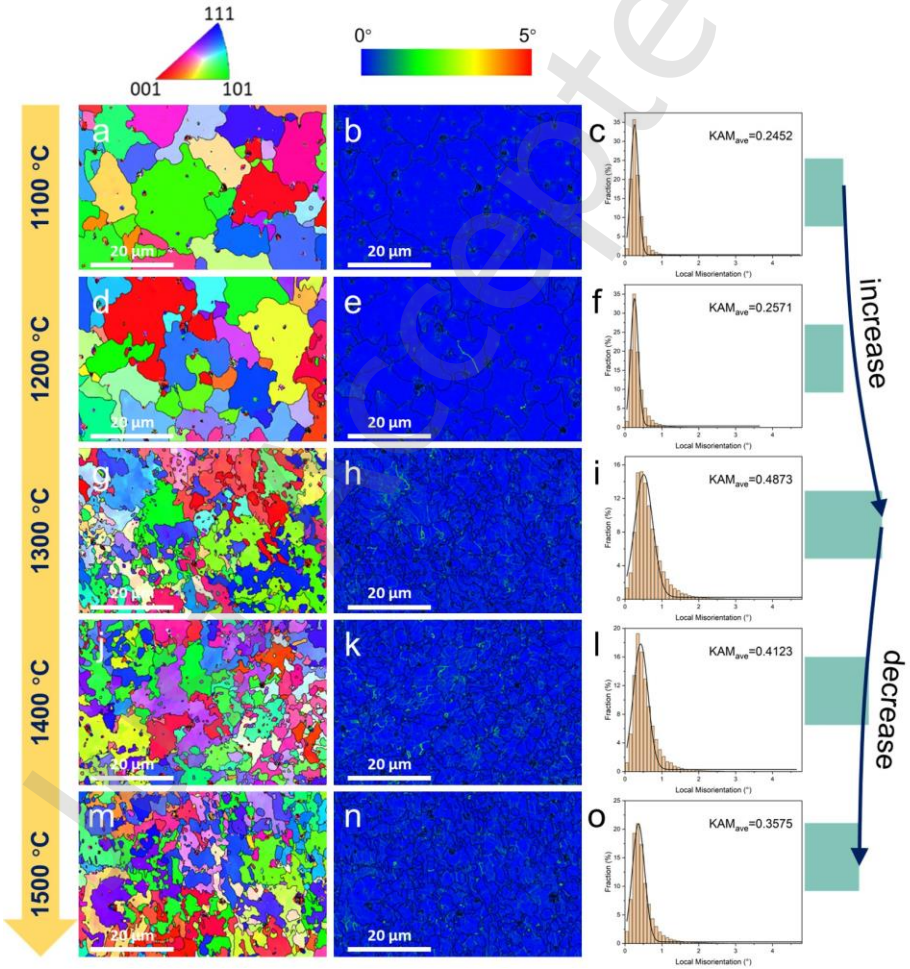

Figure 3. EBSD analysis of (Ti, Zr, V, Nb, Mo)C high-entropy ceramics aged for 20 h at different temperatures: (a, d, g, j, m) IPF maps showing grain evolution; (b, e, h, k, n) KAM maps and their corresponding distributions; and (c, f, i, l, o) evolution of the KAM_{ave} density.

To quantitatively evaluate the contribution of dislocation strengthening, a regression analysis

between the Vickers hardness (H_V) and the square root of the dislocation density ($\rho^{1/2}$) was performed based on the Taylor hardening model. As shown in **Figure S7**, the linear correlation supports an important contribution of dislocation-mediated hardening to the hardness evolution.

3.2 Multi-scale Synergistic Strengthening Mechanism

The sample aged at 1300 °C for 20 h was selected for detailed TEM analysis because it shows both a representative coexisting microstructure of spinodal decomposition domains and ZrC-rich precipitates and the best balance between hardness and fracture toughness. To gain deep insight into the micro-mechanisms responsible for this performance enhancement, detailed TEM analysis was therefore conducted on this sample. As shown in **Figure 4(a)**, the STEM-HAADF image and the corresponding EDS elemental maps confirm the three-phase coexisting composite microstructure at the meso-scale: a bright-and-dark interwoven spinodal decomposition structure and dispersed precipitates. Correlated with the EDS signals, the bright-contrast regions are identified as the (Zr, Nb)C-rich phase, while the gray-contrast regions are identified as the (Ti, V, Mo)C-rich phase. These two phases constitute the spinodal decomposition structure. Meanwhile, the spherical precipitates, which exhibit a deep-black contrast, are confirmed to be a ZrC-rich phase. This result, at the meso-scale, corroborates the SEM observations and is consistent with the thermodynamic prediction that the high-temperature FCC solid solution separates into (Zr, Nb)C-rich and (Ti, V, Mo)C-rich carbide phases during aging. In addition to this phase-separation process, ZrC-rich precipitates are directly identified by SEM and TEM analyses. Their formation is driven by local Zr enrichment during aging and precipitation from the supersaturated FCC solid solution under finite-time kinetic conditions.

The nature of the interfaces is central to determining the strengthening efficacy [58]. **Figure 4**

provides a detailed analysis of the interfacial relationships between the different phases. For the (Ti, V, Mo)-rich and (Zr, Nb)-rich phases formed by spinodal decomposition (**Figures 4(b-g)**), the HRTEM image reveals a lattice constant mismatch between them, with lattice spacings of approximately 0.221 nm and 0.228 nm, respectively. However, the Selected Area Electron Diffraction (SAED) patterns from both sides correspond to the [0 -1 1] zone axis, indicating that the two phases share the same crystallographic orientation. This interface, characterized by a shared orientation but different lattice constants, relieves strain by introducing periodic misfit dislocations, thus forming a typical semi-coherent interface. Geometric Phase Analysis (GPA) strain mapping also confirms the existence of significant strain concentration at this interface. In contrast, for the interface between the ZrC-rich precipitate and the surrounding spinodal phase (**Figures 4(h-k)**), the comparison with the standard diffraction spots is shown in **Figure S8**, the SAED patterns from the two sides do not share the same zone axis. This indicates a lack of a specific orientation relationship, resulting in the formation of a fully incoherent interface.

The semi-coherent interface, with its periodic array of misfit dislocations, introduces a long-range elastic strain field that effectively impedes the long-range glide of dislocations [59,60]. The incoherent interface, conversely, acts as a short-range pinning obstacle with high stress concentration due to the mismatched crystallographic orientations and the discontinuity in atomic arrangement [61,62]. This structure strongly pins dislocations and forces crack-tip deflection. This synergistic obstacle system—comprising long-range strain fields (from the spinodal phases) and short-range strong pinning sites (from the precipitates)—provides a dense and highly effective composite barrier network for impeding both dislocation motion and crack propagation [63,64].

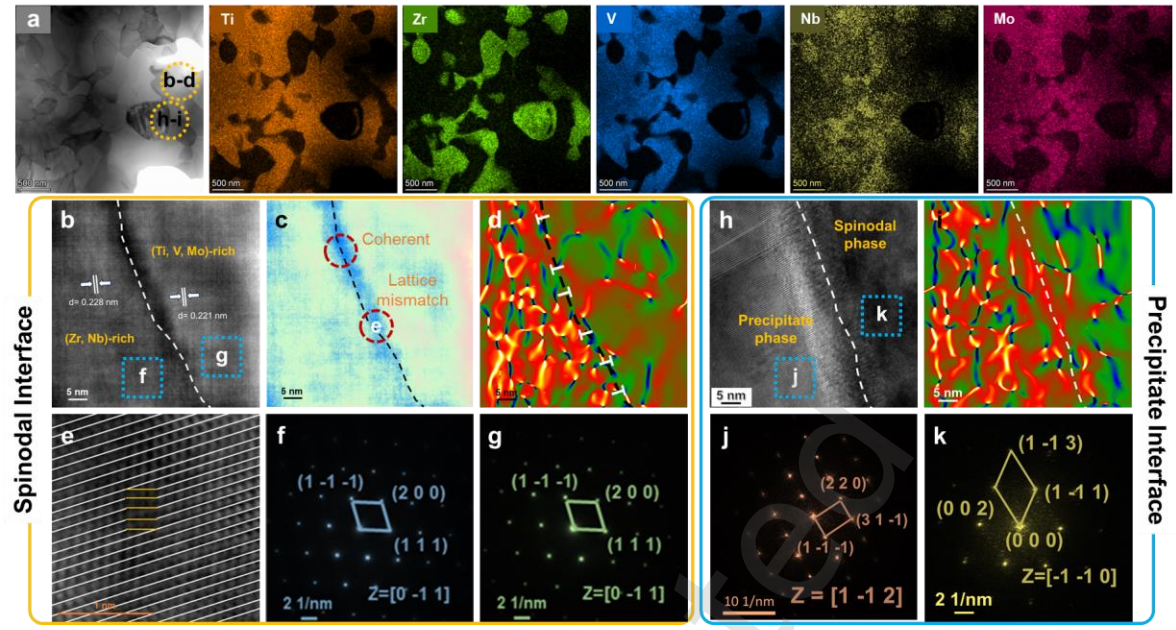

Figure 4. Interface engineering analysis of (Ti, Zr, V, Nb, Mo)C high-entropy ceramic (1300°C, 20 h), (a) STEM-HAADF image and corresponding EDS elemental maps of Ti, Zr, V, Nb, and Mo, (b) HRTEM image of the two spinodal phases, (c) corresponding IFFT image, (d) corresponding GPA strain map, (e) HRTEM image, (f, g) FFT patterns of the two spinodal phases, (h) HRTEM image of the precipitate interface, (i) corresponding GPA strain map, (j) FFT pattern of the precipitate phase, (k) FFT pattern of the spinodal phase.

In addition to interface strengthening, a high density of intragranular defects is present in the aged samples. As illustrated in **Figures 5(a-i)**, extremely high-density defect structures are observed within the spinodal matrix, particularly in the vicinity of the semi-coherent interfaces. These defects manifest in two primary forms: discrete dislocation lines (**Figures 5(a-d)**) and interconnected dislocation networks (**Figures 5(e-i)**). The discrete dislocation lines are identified as mobile dislocations generated to relax local, transient coherency strains during the dynamic progression of spinodal decomposition [10,65]. Both IFFT and GPA analyses clearly reveal their dislocation cores and the associated strong, localized strain fields. The dislocation networks, in contrast, are primarily misfit dislocations that

accumulate at or near the semi-coherent interfaces during the phase separation process to accommodate the final lattice mismatch between the (Ti, V, Mo)C-rich and (Zr, Nb)C-rich phases [66]. IFFT and GPA analyses also vividly visualize the significant dislocation pile-up effects and the generation of pronounced stress-strain phenomena in these regions. These two types of dislocation structures—originating from different causes but both induced by the phase transformation—intertwine with the semi-coherent interfaces. Together, they constitute the microscopic mechanism responsible for achieving both high hardness and high toughness. On one hand, they form a dense barrier that impedes subsequent dislocation slip, a key source of the material's high hardness consistent with the Taylor hardening model [67,68]. On the other hand, during crack propagation, these complex interface and defect structures effectively dissipate energy by inducing crack deflection and activating dislocations, which leads to crack-tip blunting, thereby significantly enhancing the material's toughness [69].

In contrast to the spinodal decomposition in the matrix, the ZrC-rich precipitates exhibit another unique defect strengthening mechanism (**Figures 5(j-r)**). HRTEM characterization confirms that these precipitates are not perfect single crystals but are inherently rich in high-density nanotwins (**Figures 5(j-m)**). Their corresponding FFT diffraction pattern (**Figure 5(l)**) also presents a typical symmetric arrangement of spots across the twin plane. These high-density twin boundaries are themselves potent lattice defects. Much like grain boundaries, they effectively impede dislocation motion, contributing to hardness by reducing the effective mean free path for dislocation slip [70,71]. Concurrently, the interaction of twin boundaries with dislocations, as well as the plastic deformation of the twins themselves under applied stress, serve as crucial energy dissipation pathways within the crack-tip plastic zone, thereby significantly enhancing the material's toughness [72,73]. Furthermore, a high

density of stacking faults was observed between the nanotwins (**Figures 5(o-r)**), causing a distinct streaking or elongation phenomenon in the FFT spots (**Figure 5(q)**). As a type of planar defect, stacking faults markedly increase the resistance to dislocation slip and effectively pin dislocations [74,75]. They act synergistically with the nanotwin boundaries, not only further strengthening the precipitate interior but also providing an additional avenue for energy dissipation, thus positively contributing to both the hardness and toughness of the material [76,77].

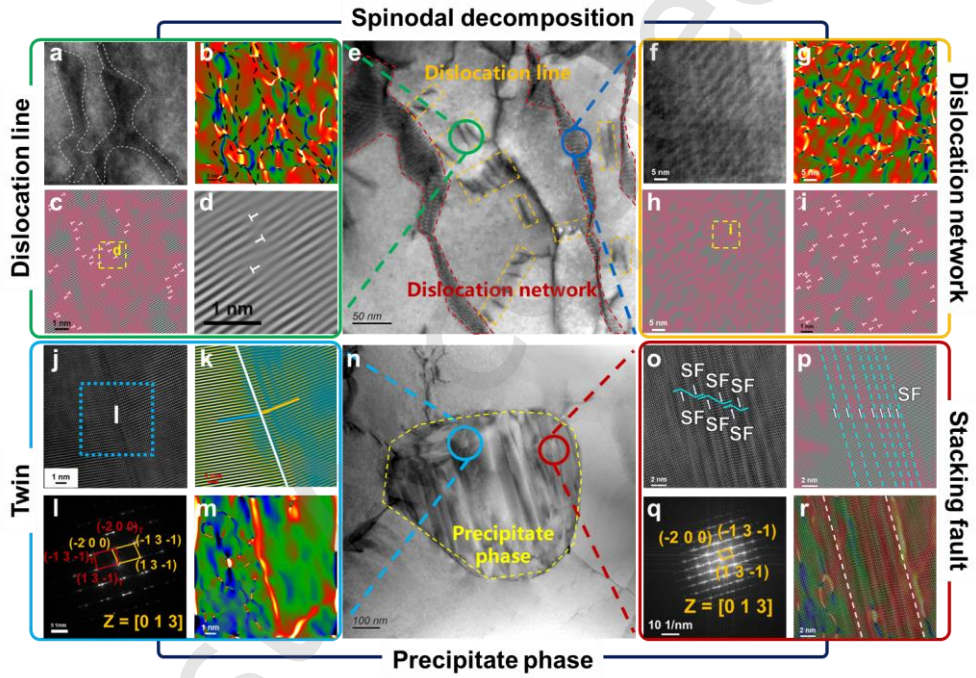

Figure 5. Defect engineering analysis of (Ti, Zr, V, Nb, Mo)C high-entropy ceramic (1300°C, 20 h). (a) Dislocation line morphology, (b) corresponding GPA strain map, (c) IFFT image, (d) magnified dislocation core, (e) morphology, (f) corresponding HRTEM image, (g) GPA strain map, (h-i) IFFT images, (j) nanotwin HRTEM image, (k) corresponding IFFT image, (l) nanotwin FFT pattern, (m) nanotwin GPA strain map; (n) morphology, (o) stacking fault HRTEM image, (p) corresponding IFFT image, (q) stacking fault FFT pattern, (r) stacking fault GPA strain map.

Previous studies have shown that twin formation in ZrC-based carbides can be influenced by C

vacancies. Hu et al. [78] induced twin structures in ZrC by regulating C vacancies and further demonstrated by first-principles calculations that C vacancies can significantly reduce the twin-boundary energy of ZrC, thereby facilitating the formation and stabilization of twin structures.

To further clarify the chemical characteristics of the ZrC-rich precipitates, STEM-EDS elemental mapping was supplemented, as shown in **Figure S9**. The precipitate region exhibits pronounced Zr enrichment, while no obvious O enrichment is observed, indicating that ZrO_2-related oxides are unlikely to be the dominant precipitated phase. Meanwhile, the C signal in the Zr-enriched region is relatively weakened compared with the surrounding matrix, demonstrating that the ZrC-rich precipitates possess certain C-vacancy or local non-stoichiometric characteristics. Based on this observation, first-principles calculations were further performed to evaluate the effect of C vacancies on the planar defect energies of ZrC, with the calculation details and specific analysis provided in **Section S3** of the Supporting Information. As shown in **Figure S10**, increasing C-vacancy concentration reduces the twin-boundary energy and stacking-fault energy of ZrC, indicating that C vacancies can lower the energetic cost for planar defect formation and thus facilitate the formation of stacking faults and nanotwins in the ZrC-rich precipitates.

3.3 Macroscopic Mechanical Performance and Analysis

The evolution of the microstructure, particularly the formation of phase-separated domains and ZrC-rich precipitates, is expected to influence the fracture behavior of the material [79-81]. **Figure 6** shows representative indentation-induced crack propagation paths in samples aged for 20 h at different temperatures. The indentation morphology in **Figure 6(a)** shows cracks emanating from the indentation corners. In the aged samples, local changes in the crack propagation path can be observed

near heterogeneous microstructural regions, including phase-separated domains and ZrC-rich precipitates. These features introduce heterogeneous interfaces with differences in composition, lattice structure, and local strain state, which may perturb the crack-tip stress field and promote local crack-path deviation or crack pinning during propagation. Such crack-path perturbation may contribute to fracture-energy dissipation and improved fracture resistance in the aged ceramics.

Crack-path perturbation and crack pinning are common energy-dissipation mechanisms in ceramic materials [79,82,83]. In the present system, the semi-coherent interfaces generated by spinodal decomposition and the incoherent interfaces associated with ZrC-rich precipitates provide heterogeneous regions that can interact with propagating cracks [84]. In addition to these interfacial effects, the aging-induced dislocation networks, nanotwins, and stacking faults can further contribute to crack-tip blunting and defect-mediated energy dissipation. Therefore, the enhanced fracture toughness after aging is attributed to the combined effects of interfacial blocking, local crack-path perturbation, and defect-assisted energy dissipation, rather than to crack deflection alone.

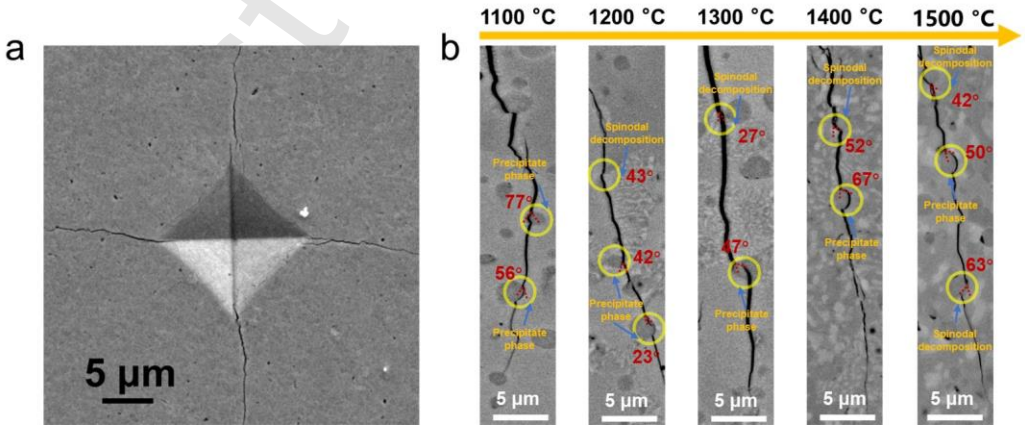

Figure 6. Crack propagation paths in (Ti, Zr, V, Nb, Mo)C high-entropy ceramic, (a) typical Vickers indentation crack morphology of the sample aged at 1300 °C for 20 h, (b) representative indentation-induced crack propagation paths in samples aged at 1100–1500 °C for 20 h, the yellow circles mark

local crack-path changes near heterogeneous microstructural regions.

Figure 7(a) and **Figure 7(b)** show the evolution of Vickers hardness and fracture toughness, respectively, for the (Ti, Zr, V, Nb, Mo)C ceramics as a function of aging temperature and time. As shown in **Figure 7(a)**, the hardness evolution exhibits a monotonic increase at lower aging temperatures. At 1100 °C, the hardness slowly increases with time, showing a 12% enhancement after 50 h compared to the as-sintered state. At 1200 °C, the growth rate accelerates, and the hardness increases by 23% after 50 h. However, when the aging temperature is elevated to 1300 °C and 1400 °C, the hardness evolution displays a phenomenon of first increasing and then decreasing. At 1300 °C, the hardness reaches its peak value at 20 h, an increase of 36%, before subsequently decreasing. At 1400 °C, the hardness peaks at 20 h with a 35% increase compared to the initial state, but it also drops after being extended to 50 h. When the temperature reaches 1500 °C, the performance decline occurs earlier. The hardness peaks at 10 h (a 26% increase) and then continuously decreases at 20 h and 50 h.

The evolution of fracture toughness, shown in **Figure 7(b)**, exhibits a highly consistent synergistic trend with hardness. At 1100 °C and 1200 °C, the toughness monotonically increases with aging time, showing 18% and 31% increases, respectively, at 50 h. At 1300 °C and 1400 °C, the toughness also shows a behavior of first increasing and then decreasing. Notably, the sample aged at 1300 °C for 20 h achieves the highest fracture toughness in the entire experiment, with a 45% increase over the as-sintered state. At 1400 °C, the toughness peak also occurs at 20 h, with a 42% increase. At 1500°C, the performance decline is premature, with the peak occurring at 10 h (a 12% increase), followed by a continuous decrease in toughness. The specific values of hardness and fracture toughness are presented in **Table S2** and **Table S3**

In summary, the hardness and toughness of the (Ti, Zr, V, Nb, Mo)C ceramics achieve a remarkable simultaneous enhancement during the aging process. In the 1100–1200°C range, performance monotonically increases with time due to insufficient kinetics and incomplete phase transformation. In the 1300–1500°C range, a significant performance evolution of first increasing and then decreasing is observed.

The optimal processing window in this study is identified as aging at 1300 °C for 20 h. Under this condition, the material simultaneously obtains the highest fracture toughness and peak hardness, corresponding to increases of 45% and 36%, respectively, compared with the as-sintered state. This increase-then-decrease trend is consistent with the EBSD results in **Figure 3**, where the KAM_{ave} value reaches a maximum at 1300 °C and then decreases at 1400–1500 °C. This strongly confirms that the material's strengthening and toughening originate from the multi-scale defect structures induced by aging, including interfaces, dislocations, and twins. When the aging time is too long (e.g., 50 h) or the temperature is too high (e.g., 1500 °C), the microstructure (both spinodal and precipitate phases) undergoes coarsening (as shown in **Figure 2**). Concurrently, the high temperature leads to the recovery and annihilation of dislocations (as shown in **Figure 3**). These two mechanisms jointly lead to the weakening of the strengthening effect, causing both hardness and toughness to drop from their peak values [85,86].

To evaluate the effectiveness of the synergistic strengthening strategy in this study, **Figure 7(c)** compares the optimal performance obtained in this work (indicated by the red star) against the hardness-toughness data of other high-entropy ceramics reported in the literature [6,7,20,87-91]. As shown, the reported hard ceramic materials generally exhibit a trade-off relationship between hardness

and fracture toughness, where higher hardness is often accompanied by lower fracture toughness. However, the (Ti, Zr, V, Nb, Mo)C ceramic prepared in this work *via* the synergistic strategy of spinodal decomposition and precipitation strengthening achieves a fracture toughness far superior to similar materials while maintaining ultra-high hardness. Its data point (the red star) significantly deviates from and surpasses the performance boundary of traditional materials, fully demonstrating the immense potential of this synergistic strategy in overcoming the intrinsic brittleness of materials.

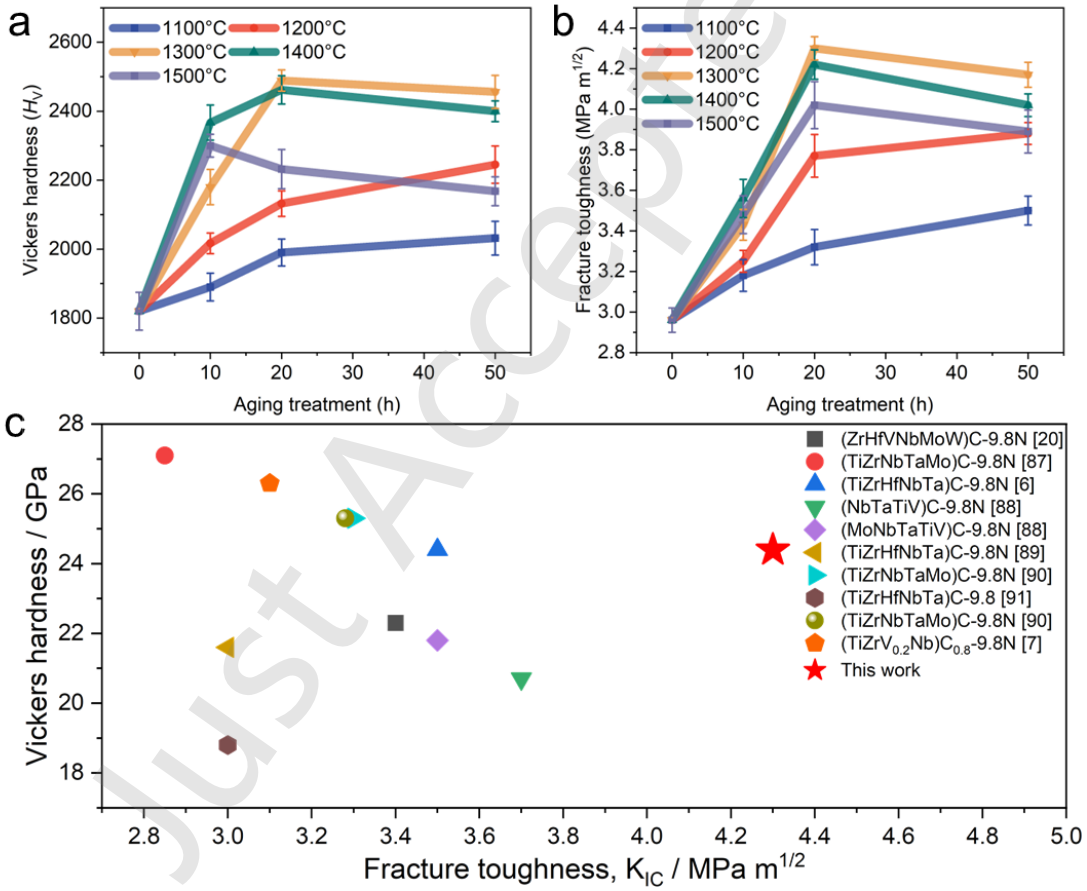

Figure 7. Mechanical property evolution and comparison for the (Ti, Zr, V, Nb, Mo)C ceramic. (a) Vickers hardness and (b) fracture toughness as a function of aging temperature and time, (c) hardness-toughness comparison plot of this work (red star) against reported high-entropy ceramics and spinodal decomposition-strengthened ceramics from the literature.

In summary, as schematically illustrated in **Figure 8**, the strengthening mechanism of the (Ti, Zr, V, Nb, Mo)C ceramic is a complex synergistic effect that spans the atomic, micro, and meso scales. This effect originates at the atomic scale with interface engineering, which is founded upon the semi-coherent (Ti, V, Mo)C-rich / (Zr, Nb)C-rich interfaces from spinodal decomposition and the incoherent ZrC-rich precipitate interfaces [59-62]. At the micro-scale, these two types of interfaces induce defect engineering [92]: first, the lattice mismatch stress from the semi-coherent interfaces generates a high-density dislocation network within the spinodal matrix [59-62], and second, the observed ZrC-rich precipitates contain abundant nanotwins and stacking faults [70,71]. Ultimately, at the meso-scale, these defect structures form the resulting architecture of phase transformation engineering, namely, the spinodal decomposition network and the precipitates. This hierarchical strengthening system, spanning from the atomic to the meso-scale, finally endows the material with a synergistic enhancement of hardness and toughness at the macroscopic scale, successfully mitigating the hardness-toughness trade-off [93]. Distinct from the external introduction of zirconia or low-melting-point phases that often leads to thermal instability or hardness degradation, this in-situ phase separation strategy constructs a fully refractory hierarchical architecture [94]. This intrinsic design not only ensures exceptional high-temperature stability but also effectively breaks the traditional trade-off between hardness and toughness through multi-scale synergy.

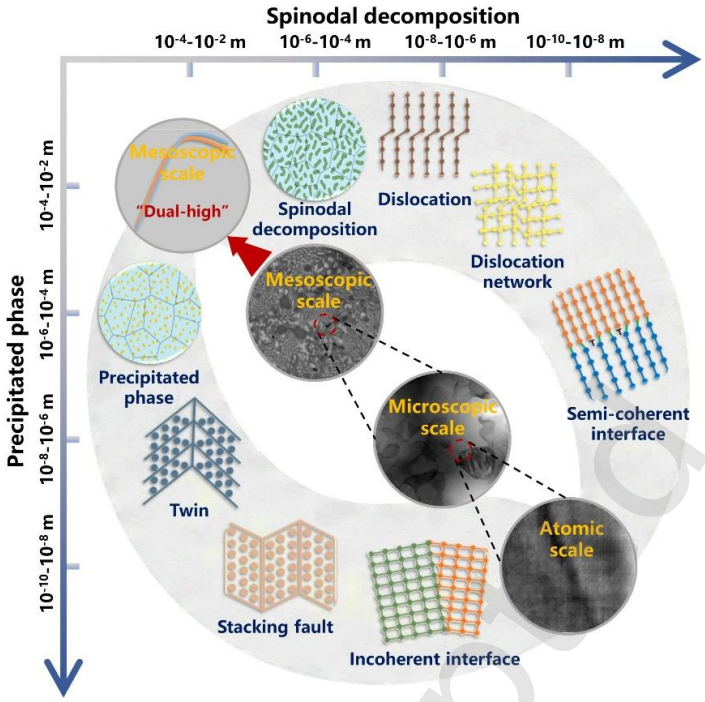

Figure 8. Schematic illustration of the multi-scale synergistic strengthening mechanism in the (Ti, Zr, V, Nb, Mo)C high-entropy ceramic.

4. Conclusion

To address the hardness–toughness trade-off in high-entropy carbides, (Ti, Zr, V, Nb, Mo)C was selected as a model system and subjected to SPS followed by aging treatments to regulate its metastable phase-transformation behavior. The as-sintered single-phase FCC solid solution underwent coupled spinodal decomposition and precipitation during aging, forming a spinodal decomposition structure consisting of (Ti, V, Mo)C-rich and (Zr, Nb)C-rich phases together with Zr-rich rock-salt carbide precipitates, referred to as ZrC-rich precipitates. This coexisting microstructure constructed a multi-scale strengthening and toughening architecture, in which semi-coherent spinodal interfaces and incoherent precipitate/matrix interfaces promoted local strain fields and defect formation, while the interconnected spinodal decomposition domains and dispersed precipitates jointly impeded dislocation motion and deflected crack propagation. As a result, the material achieved simultaneous enhancement

in hardness and fracture toughness. The sample aged at 1300 °C for 20 h exhibited the best overall mechanical performance, with hardness and fracture toughness increasing by 36% and 45%, respectively, compared with the as-sintered state. These results demonstrate that the coordinated control of spinodal decomposition and precipitation provides an effective strategy for constructing hierarchical microstructures and mitigating the hardness–toughness trade-off in transition-metal carbide ceramics.

Competing interests

The authors have no competing interests to declare that are relevant to the content of this article.

Acknowledgments

This work was supported by the National Key Research and Development Program of China (Grant No. 2023YFB3712600).

Reference

[1] Chen L, Zhang W, Lu W et al. Low thermal conductivity of dense (TiZrHfVNbTa)C_x high-entropy carbides by tailoring carbon stoichiometry. *J. Adv. Ceram.* 2023, **12**: 49-58.

[2] Gu W, Yang B, Li D et al. Accelerated design of lead-free high-performance piezoelectric ceramics with high accuracy via machine learning. *J. Adv. Ceram.* 2023, **12**: 1389-1405.

[3] Zhu Z, Liu Y, Qin Y et al. Tough and strong bioinspired high-entropy all-ceramics with a contiguous network structure. *Nat. Commun.* 2025, **16**: 4587.

[4] Li Y, He L, Pan H et al. Compositional optimization for enhanced oxidation resistance of high-entropy carbide ceramics. *Acta Mater.* 2025, **282**: 120463.

[5] Cai F, Ni D, Bao W et al. Ablation behavior and mechanisms of Cf/($Ti_{0.2}Zr_{0.2}Hf_{0.2}Nb_{0.2}Ta_{0.2}$)C–SiC high-entropy ceramic matrix composites. *Compos. Part B Eng.* 2022, **243**: 110177.

[6] Feng L, Chen W-T, Fahrenholtz WG et al. Strength of single-phase high-entropy carbide ceramics up to 2300°C. *J. Am. Ceram. Soc.* 2021, **104**: 419-427.

[7] Kong Q, Chen L, Huo S et al. Phase transition of multi-component (TiZrVNb)C ceramics—Part II: From single phase to multiple phases via adjusting V content. *J. Adv. Ceram.* 2024, **13**: 689-698.

[8] Ni D, Cheng Y, Zhang J et al. Advances in ultra-high temperature ceramics, composites, and coatings. *J. Adv. Ceram.* 2022, **11**: 1-56.

[9] Cao Z, Sun J, Meng L et al. Progress in densification and toughening of high entropy carbide ceramics. *J. Mater. Sci. Technol.* 2023, **161**: 10-43.

[10] Zhang Z, Guan Y, Huang Q et al. Insight of the microstructure evolution and performance enhancement of spinodal decomposition in (Ti, Zr)C composite carbide ceramics: Multiscale simulation and experimental investigation. *Acta Mater.* 2025, **282**: 120487.

[11] Yue YH, Gao YF, Hu WT et al. Hierarchically structured diamond composite with exceptional toughness. *Nature* 2020, **582**: 370-374.

[12] Kadirvel K, Fraser HL & Wang YZ. Microstructural design via spinodal-mediated phase transformation pathways in high-entropy alloys (HEAs) using phase-field modelling. *Acta Mater.* 2023, **243**: 118438.

[13] Li Y, Katsui H & Goto T. Effect of heat treatment on the decomposition of TiC-ZrC solid solutions

by spark plasma sintering. *J. Eur. Ceram. Soc.* 2016, **36**: 3795-3800.

[14] Holleck H. Ternäre carbidsysteme der actinoiden mit den übergangsmetallen der 4. bis 8. gruppe. *J. Nucl. Mater.* 1984, **124**: 129-146.

[15] Kong Q, Zhang R, Chen L et al. Phase transition of multi-component (TiZrVNb)C ceramics—Part I: The phase decomposition induced by carbon content. *J. Adv. Ceram.* 2024, **13**: 679-688.

[16] Xu L, Guo W-M, Zou J et al. Low-temperature densification of high entropy diboride based composites with fine grains and excellent mechanical properties. *Compos. Part B Eng.* 2022, **247**: 110331.

[17] Zhang Z, Guan Y, Mao H et al. Multiscale phase-field simulation framework for spinodal decomposition behavior in composite carbide ceramics. *J. Mater. Sci. Technol.* 2026, **246**: 58-75.

[18] Zhang Z, Hou C, Zhang Z et al. Data-driven design of spinodal decomposition in (Ti, Zr, Hf)C composite carbides for optimizing the hardness-toughness trade-off. *Adv. Funct. Mater.* 2025, **35**: 2502555.

[19] Zhang Z, Zhang Z, Chang G et al. Nitrogen-induced stacking fault energy reduction enables spinodal-decomposition-driven toughening in (Ti,Zr)C ceramics. *J. Adv. Ceram.* 2025, **14**: 9221188.

[20] Zhang W, Li K, Chen L et al. The phase decomposition in non-equimolar $(ZrHfVNbMoW)C_x$ complex concentrated carbides via carbon content regulation. *J. Eur. Ceram. Soc.* 2024, **44**: 1396-1403.

[21] Jiao ZC, Hua DP, Zhou Q et al. Super-hard refractory high entropy alloy film with spinodal decomposition. *J. Mater. Sci. Technol.* 2025, **213**: 190-195.

[22] Ahmadi MR, Povoden-Karadeniz E, Öksüz KI et al. A model for precipitation strengthening in multi-particle systems. *Comput. Mater. Sci.* 2014, **91**: 173-186.

[23] Zhang GH, Zhu ZW, Ning JG et al. Dynamic impact constitutive relation of 6008-T6 aluminum alloy based on dislocation density and second-phase particle strengthening effects. *J. Alloys Compd.* 2023, **932**: 167718.

[24] Tan XN, Zhang JL, Li FT et al. Tailored precipitation assisted by laser-induced cellular dislocation network structures in $Al_{0.3}$CoCrFeNi high entropy alloy. *Mater. Sci. Eng. A* 2024, **913**: 147057.

[25] Bian YJ, Wang RC, Yang F et al. Mechanical properties of internally hierarchical multiphase lattices inspired by precipitation strengthening mechanisms. *ACS Appl. Mater. Interfaces* 2023, **15**: 15928-15937.

[26] Xiang HM, Xing Y, Dai FZ et al. High-entropy ceramics: Present status, challenges, and a look forward. *J. Adv. Ceram.* 2021, **10**: 385-441.

[27] Akrami S, Edalati P, Fuji M et al. High-entropy ceramics: Review of principles, production and applications. *Mater. Sci. Eng. R* 2021, **146**: 100644.

[28] Hou X, Li CL, Gou TCX et al. Improvement of microwave dielectric properties of (Ca, Sr)TiO_3-based ceramics by high-entropy design. *J. Am. Ceram. Soc.* 2025, **108**: e20630.

[29] Hong WC, Chen F, Shen Q et al. Microstructural evolution and mechanical properties of (Mg,Co,Ni,Cu,Zn)O high-entropy ceramics. *J. Am. Ceram. Soc.* 2019, **102**: 2228-2237.

[30] Sundman B, Jansson B & Andersson J-OJC. The thermo-calc databank system. *Calphad* 1985, **9**: 153-190.

[31] Peng Y, Du Y, Zhou P et al. CSUTDCC1—A thermodynamic database for multicomponent cemented carbides. *Int. J. Refract. Met. Hard Mater.* 2014, **42**: 57-70.

[32] Anstis GR, Chantikul P, Lawn BR et al. A critical evaluation of indentation techniques for

measuring fracture toughness: 1. Direct crack measurements. *J. Am. Ceram. Soc.* 1981, **64**: 533-538.

[33] Richetta M & Varone A. A focus on dynamic modulus: Effects of external and internal morphological features. *Metals* 2021, **11**: 40.

[34] Li Y, Katsui H & Goto T. Phase decomposition of (Ti, Zr)(C, N) solid solutions prepared by spark plasma sintering. *J. Eur. Ceram. Soc.* 2019, **39**: 4588-4594.

[35] Cheng EJ, Li Y, Sakamoto J et al. Mechanical properties of individual phases of ZrB_2-ZrC eutectic composite measured by nanoindentation. *J. Eur. Ceram. Soc.* 2017, **37**: 4223-4227.

[36] Kresse G & Furthmuller J. Efficient iterative schemes for ab initio total-energy calculations using a plane-wave basis set. *Phys. Rev. B* 1996, **54**: 11169-11186.

[37] Blöchl PE, Först CJ & Schimpl J. Projector augmented wave method: ab initio molecular dynamics with full wave functions. *Bull. Mater. Sci.* 2003, **26**: 33-41.

[38] Perdew JP, Burke K & Ernzerhof M. Generalized gradient approximation made simple *Phys. Rev. Lett.* 1997, **78**: 1396-1396.

[39] A. Pandey SD, S. Dutta. Structural characterization of polycrystalline thin films by X-ray diffraction techniques. *J. Mater. Sci. Mater. Electron.* 2021, **32**: 1341-1368.

[40] Pope CG. X-ray diffraction and the Bragg equation. *J. Chem. Educ.* 1997, **74**: 129.

[41] Kim H-I, Kim T-W, Kim Y-O et al. Age-hardenability and related microstructural changes during and after phase transformation in an Au-Ag-Cu-based dental alloy. *Mater. Res.* 2013, **16**: 71-78.

[42] Van Westen T & Groot RD. Effect of temperature cycling on ostwald ripening. *Cryst. Growth Des.* 2018, **18**: 4952-4962.

[43] Zhu WD, Bao CX, Wang YRQ et al. Coarsening of one-step deposited organolead triiodide

perovskite films via Ostwald ripening for high efficiency planar-heterojunction solar cells. *Dalton Trans.* 2016, **45**: 7856-7865.

[44] Rieger T, Joubert JM, Poulain R et al. Influence of chemical composition on coarsening kinetics of coherent L12 precipitates in FCC complex concentrated alloys. *J. Alloys Compd.* 2023, **967**: 171711.

[45] Zaiser E, Fantin A, Manzoni AM et al. Elucidating hierarchical microstructures in high entropy superalloys: An integrated multiscale study. *Mater. Charact.* 2025, **220**: 114642.

[46] Brailsford AD & Wynblatt P. The dependence of ostwald ripening kinetics on particle volume fraction. *Acta Metall.* 1979, **27**: 489-497.

[47] Barriobero-Vila P, Oliveira VB, Schwarz S et al. Tracking the α" martensite decomposition during continuous heating of a Ti-6A1-6V-2Sn alloy. *Acta Mater.* 2017, **135**: 132-143.

[48] Yuan JL, Wu YC, Liaw PK et al. Remarkable cryogenic strengthening and toughening in nano-coherent CoCrFeNiTi0.2 high-entropy alloys via energetically-tuning polymorphous precipitates. *Mater. Sci. Eng. A* 2022, **842**: 143111.

[49] Xu W, Zhong YM, Li XY et al. Stabilizing supersaturation with extreme grain refinement in spinodal aluminum alloys. *Adv. Mater.* 2024, **36**: 2303650.

[50] Peng J, Wang RC, Zhu MX et al. 2430% Superplastic strain in a eutectic Au-Sn alloy with micrometer-sized grains maintained by spinodal-like decomposition. *Acta Mater.* 2022, **228**: 117766.

[51] Liu XS, Li R, Lu Y et al. Spinodal decomposition induced nanoprecipitates strengthened CoCrNi-base medium entropy alloy. *Mater. Sci. Eng. A* 2021, **822**: 141674.

[52] Wang N, Ji YZ, Wang YB et al. Two modes of grain boundary pinning by coherent precipitates. *Acta Mater.* 2017, **135**: 226-232.

[53] Hu GW, Zeng LC, Du H et al. Combined effects of solute drag and Zener pinning on grain growth of a NiCoCr medium-entropy alloy. *Intermetallics* 2021, **136**: 107271.

[54] Mohammed ASK & Sehitoglu H. Thermodynamic rationale for transformation-induced dislocations in shape memory alloys. *Acta Mater.* 2024, **274**: 119998.

[55] Long HB, Wei H, Liu YN et al. Effect of lattice misfit on the evolution of the dislocation structure in Ni-based single crystal superalloys during thermal exposure. *Acta Mater.* 2016, **120**: 95-107.

[56] Xia WS, Zhao XB, Yue L et al. Microstructural evolution and creep mechanisms in Ni-based single crystal superalloys: A review. *J. Alloys Compd.* 2020, **819**: 152954.

[57] Wang PP, Cai HY, Li MZ et al. The effect of ferroelastic domains and ultrahigh-density dislocations on fracture toughness of high entropy niobates. *J. Am. Ceram. Soc.* 2024, **107**: 2533-2545.

[58] Shang CY, Zhang FM, Zhang B et al. Interface microstructure and strengthening mechanisms of multilayer graphene reinforced titanium alloy matrix nanocomposites with network architectures. *Mater. Des.* 2020, **196**: 109119.

[59] Pan AQ, Wang WY, Xie JP et al. Molecular dynamics simulations of interface structure and deformation mechanisms in metal/ceramic composites under tension. *Mech. Mater.* 2023, **184**: 104688.

[60] Vattré A & Pan E. Three-dimensional interaction and movements of various dislocations in anisotropic bicrystals with semicoherent interfaces. *J. Mech. Phys. Solids* 2018, **116**: 185-216.

[61] Yan XX, Jiang YX, Jin QQ et al. Interfacial interaction and intense interfacial ultraviolet light emission at an incoherent interface. *Nat. Commun.* 2023, **14**: 2788.

[62] Han XL, Liu P, Sun DL et al. Quantifying the role of interface atomic structure in the compressive response of Ti_2AlN/TiAl composite using MD simulations. *J. Mater. Sci.* 2019, **54**: 5536-5550.

[63] Chen S, Aitken ZH, Pattamatta S et al. Short-range ordering alters the dislocation nucleation and propagation in refractory high-entropy alloys. *Mater. Today* 2023, **65**: 14-25.

[64] Liu J, Liu CZ, Cai HY et al. Enhanced precipitate strengthening in particulates reinforced Al-Zn-Mg-Cu composites via bimodal structure design and optimum aging strategy. *Compos. Part B Eng.* 2023, **260**: 110772.

[65] Cahn JW. Hardening by spinodal decomposition. *Acta Metall.* 1963, **11**: 1275.

[66] Yang H, Zhu LG, Zhang RF et al. Influence of high stacking-fault energy on the dissociation mechanisms of misfit dislocations at semi-coherent interfaces. *Int. J. Plast.* 2020, **126**: 102610.

[67] Ting CJ & Lu HY. Hot-pressing of magnesium aluminate spinel - II. Microstructure development. *Acta Mater.* 1999, **47**: 831-840.

[68] Subedi S, Beyerlein IJ, Lesar R et al. Strength of nanoscale metallic multilayers. *Scr. Mater.* 2018, **145**: 132-136.

[69] Li P, Shao Q, Li L et al. A novel strength-energy criterion for bimaterial interface crack propagation. *Int. J. Solids Struct.* 2024, **298**: 112864.

[70] Wang YB, Wu B & Sui ML. Dynamical dislocation emission processes from twin boundaries. *Appl. Phys. Lett.* 2008, **93**: 91-93.

[71] Liang YX, Yang XF, Ming KS et al. In situ observation of transmission and reflection of dislocations at twin boundary in CoCrNi alloys. *Sci. China Technol. Sci.* 2021, **64**: 407-413.

[72] Zhang ZJ, Sheng HW, Wang ZJ et al. Dislocation mechanisms and 3D twin architectures generate exceptional strength-ductility-toughness combination in CrCoNi medium-entropy alloy. *Nat. Commun.* 2017, **8**: 14390.

[73] Wang Z, Zhao X, Li SC et al. Strengthening mechanism based on dislocation-twin interaction under room temperature multi-directional forging of AZ80 Mg alloy. *J. Mater. Res. Technol.* 2024, **29**: 3656-3672.

[74] Liebig JP, Krauss S, Göken M et al. Influence of stacking fault energy and dislocation character on slip transfer at coherent twin boundaries studied by micropillar compression. *Acta Mater.* 2018, **154**: 261-272.

[75] Huang Y, Chen Z, Meindlhumer M et al. Harvesting superior intrinsic plasticity in nitride ceramics with negative stacking fault energy. *Acta Mater.* 2025, **286**: 120774.

[76] Liu DY, Shen ZL, Ren CX et al. Enhanced high-temperature strength of austenitic steels by nanotwins and nanoprecipitates. *Scr. Mater.* 2024, **242**: 115938.

[77] Ke X, Ye JC, Pan ZL et al. Ideal maximum strengths and defect-induced softening in nanocrystalline-nanotwinned metals. *Nat. Mater.* 2019, **18**: 1207-1214.

[78] Hu WT, Liu SC, Wen B et al. {111}-specific twinning structures in nonstoichiometric $ZrC_{0.6}$ with ordered carbon vacancies. *J. Appl. Crystallogr.* 2013, **46**: 43-47.

[79] Liu F, Han X, Cui XM et al. The influence of multi-scale second-phase particles on micro-crack initiation and propagation in Al-Zn-Mg-Cu alloy. *Vacuum* 2024, **222**: 113044.

[80] Cai CH, Song RB, Wen ED et al. Effect of microstructure evolution on tensile fracture behavior of Mg-2Zn-1Nd-0.6Zr alloy for biomedical applications. *Mater. Des.* 2019, **182**: 108038.

[81] Zhang JY, Li JS, Chen Z et al. Microstructural evolution of a ductile metastable β titanium alloy with combined TRIP/TWIP effects. *J. Alloys Compd.* 2017, **699**: 775-782.

[82] Zhen Y, Wu KJ, Lu YY et al. A thermodynamically-consistent non-isothermal phase-field model

for probing evolution of crack propagation and phase transformation. *Int. J. Mech. Sci.* 2024, **270**: 109122.

[83] Emdadi A, Fahrenholtz WG, Hilmas GE et al. A modified phase-field model for quantitative simulation of crack propagation in single-phase and multi-phase materials. *Eng. Fract. Mech.* 2018, **200**: 339-354.

[84] Li XT, Sheinerman AG, Yang H et al. Theoretical modeling of toughening mechanisms in the CrMnFeCoNi high-entropy alloy at room temperature. *Int. J. Plast.* 2022, **154**: 103304.

[85] Lee JH, Park G, Oh CY et al. Effects of long-term thermal aging on mechanical properties and microstructural evolution of 17-4 PH stainless steel in simulated thermal conditions for nuclear applications. *J. Nucl. Mater.* 2025, **606**: 155628.

[86] Li X, Huang CW, Ye XW et al. Effect of aging temperatures on the microstructure and mechanical properties of TC21 forgings with basket-weave microstructure. *Mater. Charact.* 2024, **216**: 114270.

[87] Lu W, Chen L, Zhang W et al. Single-phase formation and mechanical properties of (TiZrNbTaMo)C high-entropy ceramics: First-principles prediction and experimental study. *J. Eur. Ceram. Soc.* 2022, **42**: 2021-2027.

[88] Zhang S, Qin F, Gong M et al. Microstructure, mechanical and tribological properties of high-entropy carbide (MoNbTaTiV)C_5. *Materials* 2023, **16**: 4115.

[89] Wen T, Ye B, Nguyen MC et al. Thermophysical and mechanical properties of novel high-entropy metal nitride-carbides. *J. Am. Ceram. Soc.* 2020, **103**: 6475-6489.

[90] Wang K, Chen L, Xu C et al. Microstructure and mechanical properties of (TiZrNbTaMo)C high-entropy ceramic. *J. Mater. Sci. Technol.* 2020, **39**: 99-105.

[91] Ye B, Wen T, Huang K et al. First-principles study, fabrication, and characterization of ($Hf_{0.2}Zr0_{.2}Ta_{0.2}Nb_{0.2}Ti_{0.2}$)C high-entropy ceramic. *J. Am. Ceram. Soc.* 2019, **102**: 4344-4352.

[92] Brillson LJ. Defects at nanoscale semiconductor interfaces: Challenges and opportunities. *J. Mater. Res.* 2024, **39**: 177-187.

[93] Guoa SK, Ma Z, Xiaa GH et al. Pursuing ultrastrong and ductile medium entropy alloys via architecting nanoprecipitates-enhanced hierarchical heterostructure. *Acta Mater.* 2024, **263**: 119492.

[94] Xie XF, Xie ZM, Liu R et al. Hierarchical microstructures enabled excellent low-temperature strength-ductility synergy in bulk pure tungsten. *Acta Mater.* 2022, **228**: 117765.